Supplementary Materials for Magnetic excitations of the Kitaev model candidate $RuBr_3$

Kazuhiro Nawa,[1] Yoshinori Imai,[2] Maiko Kofu,[3,4] Richard Mole,[5] Hideyuki Fujihara,[2] Takumi Hiraoka,[1,2] Ryo Murasaki,[1,*] Pharit Piyawongwatthana,[4,1] Daisuke Okuyama,[1,†] Hirotada Gotou,[3] Kenya Ohgushi,[2] and Taku J Sato[3,1]

[1]*Institute of Multidisciplinary Research for Advanced Materials, Tohoku University, Katahira 2-1-1, Sendai, 980-8577, Miyagi, Japan*
[2]*Department of Physics, Graduate School of Science, Tohoku University, Aramaki-Aoba 6-3, Sendai, 980-8578, Miyagi, Japan*
[3]*Institute for Solid State Physics, the University of Tokyo, Kashiwanoha 5-1-5, Kashiwa, 277-8581, Chiba, Japan*
[4]*Materials and Life Science Division, J-PARC Center, Japan Atomic Energy Agency, Shirakata 2-4, Tokai, 319-1195, Ibaraki, Japan*
[5]*Australian Nuclear Science and Technology Organisation, Lucas Heights, NSW 2234, Australia*

I. INELASTIC NEUTRON SCATTERING EXPERIMENTS USING AMATERAS

In the inelastic neutron scattering experiments using AMATERAS[1], excitation spectra with a few different incident neutron energies were collected simultaneously owing to a repetition rate multiplication[2]. The discussions in the main text were mainly made on the spectra collected by E_i = 20.95 meV (dE = 0.85 meV), since they well cover the energy range of the spin excitations in $RuBr_3$. In this Supplemental Information, we also present the data collected at different E_is that also support the discussion. For instance, the excitation spectra collected with E_i = 5.57 meV (dE = 0.13 meV) and E_i = 9.70 meV (dE = 0.29 meV) are appropriate for observing the low-energy spin excitations. They are shown in Figs. S1 and S2, respectively. Both excitation spectra support the existence of the dispersive spin excitations at 0.6 Å^{-1} at 10 K and the persistence of the spin excitations centered at 0.6 Å^{-1} at 45 K. In addition, the excitation spectrum was also collected with E_i = 42.17 meV (dE = 0.91 meV) to investigate the spin excitations at high energy transfer. Figure S3 represents the inelastic neutron scattering spectrum collected with E_i = 42.17 meV. The spectrum shows the dispersive spin excitations at 0.6 Å^{-1} extending up to the energy transfer of 15 meV, where weak dispersive modes were observed.

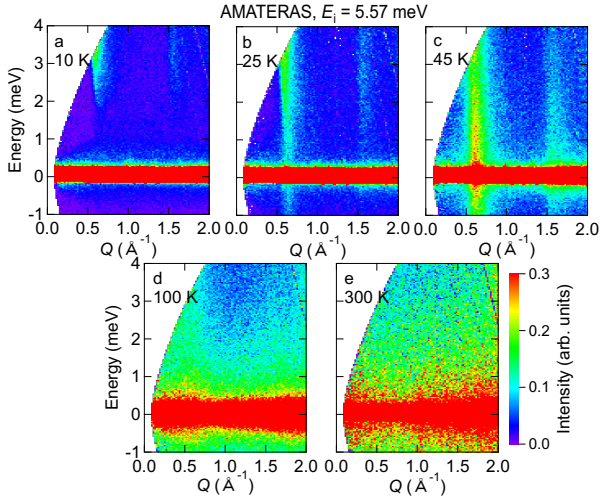

FIG. S1. Inelastic neutron scattering spectrum measured by using AMATERAS (E_i = 5.57 meV).

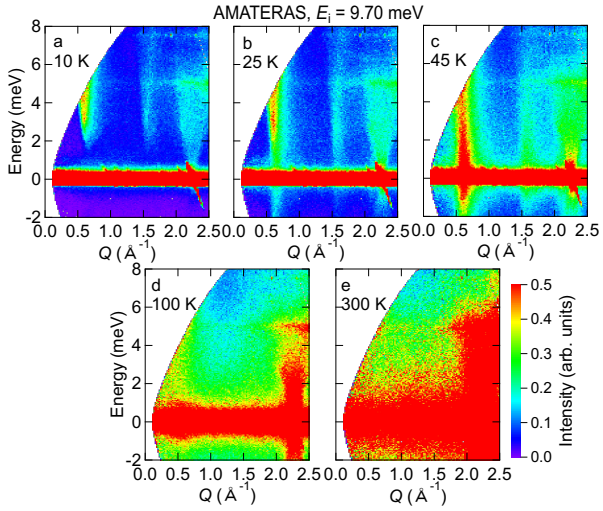

FIG. S2. Inelastic neutron scattering spectrum measured by using AMATERAS (E_i = 9.70 meV)

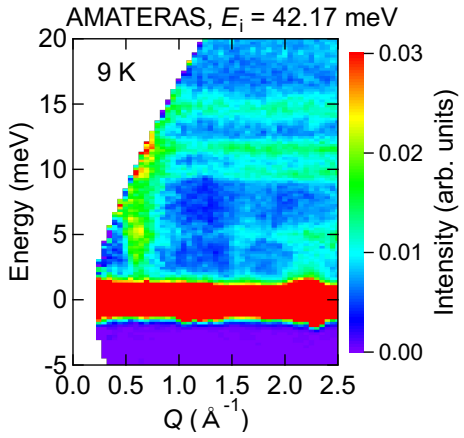

FIG. S3. Inelastic neutron scattering spectrum measured by using AMATERAS with the incident neutron energy of 42.17 meV at 9 K.

II. INELASTIC NEUTRON SCATTERING EXPERIMENTS USING PELICAN

Low-energy spin excitations were investigated by the time-of-flight spectrometer PELICAN in ANSTO[3]. Incident neutron energies were set to $E_i = 3.72$ meV with a monochromating master chopper frequency of 100 Hz. The sample was sealed in an aluminum annular sample cell with inner diameter of 20.5 mm and outer diameter of 22.5 mm. Intensities were collected at 1.5, 25, 45, and 100 K using a top loading cryostat. The collected intensities were analyzed using LAMP software suite[4]. Since the background $I(Q,E)_{bg}$ at positive energy transfer were comparable with the intensities expected from the sample, the background was estimated from the 100 K data from the deviation from the detailed balance as

$$I(Q,E)_{bg} = I(Q,E) - I(Q,-E)e^{E/(k_B T)}, \qquad \text{(S1)}$$

$I(Q,E)_{bg}$ was assumed to be temperature independent and subtracted from all the data.

Figure S4 shows the spin excitation spectrum measured at 1.5, 25, 45, and 100 K after the subtraction. At 1.5 K, spin excitations were not observed. This should be because the existence of the energy gap in the spin excitations. At 25 K, gapless spin excitations were found to develop around 0.6 Å $^{-1}$, near the magnetic reflection appears. With increasing temperature, strong wavevector dependence becomes prominent at 45 K, while it is about to spread out at 100 K. The temperature dependence is consistent with those observed in the experiments using AMATERAS.

III. NEUTRON SCATTERING EXPERIMENTS USING 4G GPTAS

The temperature dependence of the magnetic reflections and spin excitations were investigated by the

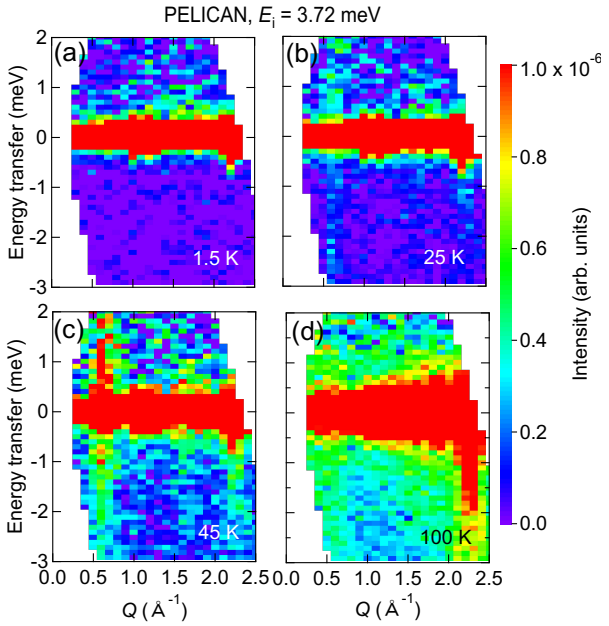

FIG. S4. (a–d) Inelastic neutron scattering spectrum measured by using PELICAN with the incident neutron energy of 3.72 meV at (a) 1.5, (b) 25, (c) 45, and (d) 100 K.

general-purpose triple-axis neutron spectrometer 4G GPTAS in JRR-3[5]. The temperature dependence of the magnetic reflections was collected by operating the spectrometer in the two-axis mode. Incident neutrons were monochromated to the wavelength of 2.36 Å using pyrolytic graphite 002 reflections and the horizontal collimations were set to 40'-40'-40'-open. A pyrolytic graphite filter was inserted in the upstream-side of the monochrometer to eliminate the higher harmonic neutrons. On the other hand, the spin excitations were collected by changing the incident neutron energy with fixing the neutron energy scattered from the sample to 14.7 meV. A pyrolytic graphite filter was inserted in the upstream-side of the analyzer to remove half-wavelength neutrons. The energy transfer and wavevector dependences were collected in the different conditions. For the energy transfer dependence, pyrolytic graphite 002 reflections were used for monochromator while 004 reflections were used for the analyzer to improve energy resolutions. Both monochromator and analyzer were set in both horizontally and vertically focusing conditions to increase efficiency. For the wavevector dependence, pyrolytic graphite 002 reflections were used for both monochromator and analyzer. The monochromator was set in both horizontally and vertically focusing conditions to increase incident neutron flux, while the analyzer was aligned in the horizontally flat condition. The horizontal collimations were set to open-RC-80'-80' (RC: radial collimator).

The transition temperature was confirmed by measuring the temperature dependence of the 0 1/2 1 magnetic reflection. Figure S5 represents the θ–2θ scans collected

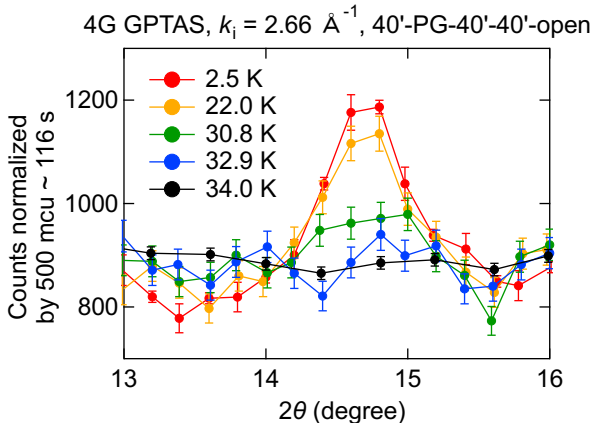

FIG. S5. θ–2θ scans collected at selected temperatures around 0 1/2 1 magnetic reflection. Magnetic reflections were collected by the incident neutron energy of 14.7 meV. The peak disappears above the transition temperature of 34 K.

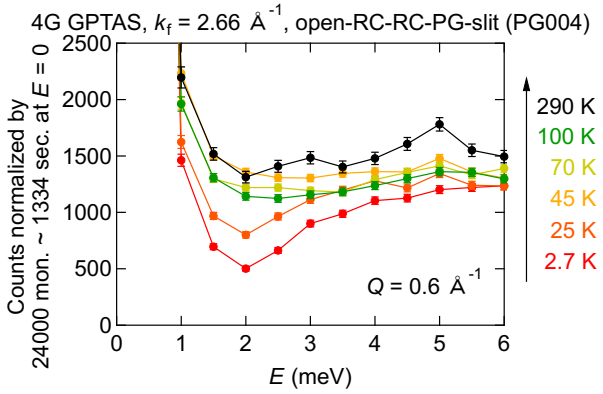

FIG. S6. Constant wavevector scan with the wavevector of 0.6 Å^{-1}. The excitation gap of 2 meV at the base temperature gets smaller with increasing temperature.

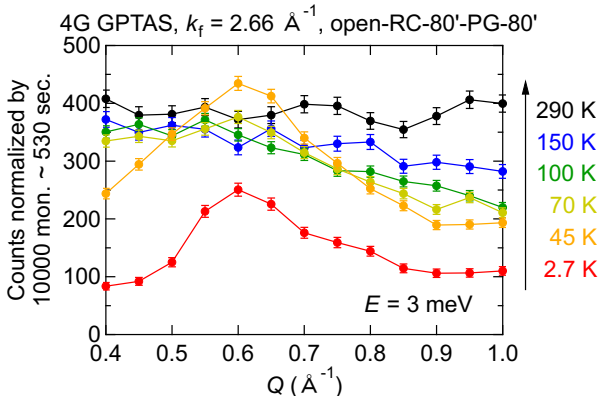

FIG. S7. Constant energy scans with the energy transfer of 3 meV. A peak at 0.6 Å^{-1} becomes broad and shifts to the lower wavevector with increasing temperature above T_N = 34 K.

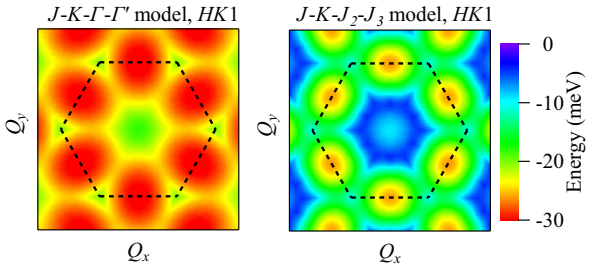

FIG. S8. Color maps of Q-dependent classical energy obtained by Luttinger-Tisza method for (a) the J_1–K–Γ–Γ' and (b) the J_1–K–J_2–J_3 models. Dashed lines indicate the Brillouin zone of a single layer honeycomb structure.

IV. LINEAR SPIN WAVE CALCULATIONS

As shown in the Methods section, linear spin wave calculations have been performed starting from the Hamiltonian eq. (2) in the main text. $RuBr_3$ includes two Ru sites in the primitive unit cell, which can be regarded as two different sublattices. They are present at the fractional coordinates (2/3, 1/3, z_{Ru}) and (1/3, 2/3, 1-z_{Ru})[6]. The z_{Ru} value of 0.0003 was approximated to be 0. In the following, the atomic position and spin operators at each sublattice A or B are defined as $\mathbf{R}_{Xi}$ and $\mathbf{S}_{Xi}$ (X = A, B), respectively.

First, the classical ground state was calculated for given parameters using the Luttinger-Tisza method[7–12]. The original problem is to minimize the total energy under the strong constraints, $\mathbf{S}_{A,i} \cdot \mathbf{S}_{A,i} - S^2 = 0$ and $\mathbf{S}_{B,i} \cdot \mathbf{S}_{B,i} - S^2 = 0$, for all magnetic site. In the Luttinger-Tisza method, the constrains are relaxed as $\sum_i (\mathbf{S}_{A,i} \cdot \mathbf{S}_{A,i} - S^2 + \mathbf{S}_{B,i} \cdot \mathbf{S}_{B,i} - S^2) = 0$. The mo-

mentum dependent form of the Hamiltonian becomes,

$$
\begin{aligned}
H &= \frac{1}{2}\mathbf{\Phi}^\dagger H_{\mathbf{k}} \mathbf{\Phi}, \\
\mathbf{\Phi} &= \begin{pmatrix} S_{A\mathbf{k}} \\ S_{B\mathbf{k}} \end{pmatrix}, \\
\mathbf{S}_{\mathrm{A}\mathbf{k}} &\equiv \frac{1}{N}\sum_i e^{-i\mathbf{k}\cdot(\mathbf{R}_{\mathrm{A}i}+\mathbf{R}_{\mathrm{A}0})}\mathbf{S}_{\mathrm{A}i}, \\
\mathbf{S}_{\mathrm{B}\mathbf{k}} &\equiv \frac{1}{N}\sum_i e^{-i\mathbf{k}\cdot(\mathbf{R}_{\mathrm{B}i}+\mathbf{R}_{\mathrm{B}0})}\mathbf{S}_{\mathrm{B}i}, \\
H_{\mathbf{k}} &\equiv \begin{pmatrix} J_{\mathrm{AA}\mathbf{k}} & J_{\mathrm{AB}\mathbf{k}} \\ J_{\mathrm{BA}\mathbf{k}} & J_{\mathrm{BB}\mathbf{k}} \end{pmatrix}, \\
J_{\mathrm{AA}\mathbf{k}} &\equiv \sum_j \mathbf{J}_{(\mathrm{A}i)(\mathrm{A}j)} e^{i\mathbf{k}\cdot(\mathbf{R}_{\mathrm{A}i}-\mathbf{R}_{\mathrm{A}j})}, \\
J_{\mathrm{AB}\mathbf{k}} &\equiv \sum_j \mathbf{J}_{(\mathrm{A}i)(\mathrm{B}j)} e^{i\mathbf{k}\cdot(\mathbf{R}_{\mathrm{A}i}-\mathbf{R}_{\mathrm{B}j}+\mathbf{R}_{\mathrm{A}0}-\mathbf{R}_{\mathrm{B}0})}, \\
J_{\mathrm{BA}\mathbf{k}} &\equiv \sum_j \mathbf{J}_{(\mathrm{B}i)(\mathrm{A}j)} e^{i\mathbf{k}\cdot(\mathbf{R}_{\mathrm{B}i}-\mathbf{R}_{\mathrm{A}j}+\mathbf{R}_{\mathrm{B}0}-\mathbf{R}_{\mathrm{A}0})}, \\
J_{\mathrm{BB}\mathbf{k}} &\equiv \sum_j \mathbf{J}_{(\mathrm{B}i)(\mathrm{B}j)} e^{i\mathbf{k}\cdot(\mathbf{R}_{\mathrm{B}i}-\mathbf{R}_{\mathrm{B}j})},
\end{aligned}
\tag{S2}
$$

while the constraints are rewritten as $\sum_{\mathbf{k}}(\mathbf{S}_{\mathrm{A},\mathbf{k}}\cdot\mathbf{S}_{\mathrm{A},-\mathbf{k}} - S^2 + \mathbf{S}_{\mathrm{B},\mathbf{k}}\cdot\mathbf{S}_{\mathrm{B},-\mathbf{k}} - S^2) = 0$ and $\sum_{\mathbf{k}}(\mathbf{S}_{\mathrm{A},\mathbf{k}}\cdot\mathbf{S}_{\mathrm{A},\mathbf{q}-\mathbf{k}} + \mathbf{S}_{\mathrm{B},\mathbf{k}}\cdot\mathbf{S}_{\mathrm{B},\mathbf{q}-\mathbf{k}}) = 0$ for all $\mathbf{q} \neq 0$. Since the constrains correspond to normalization and orthogonalization conditions of the eigenvector $\mathbf{\Phi}$, the ground state energy can be determined as the smallest eigenvalue of $H_{\mathbf{k}}$ throughout the Brillouin zone. The wavevector that minimizes $H_{\mathbf{k}}$ and the eigenvector of the smallest eigenvalue determine the ground state magnetic structure. For instance, the distribution of energy $H_{\mathbf{k}}$ on the $HK1$ plane for the J_1–K–Γ–Γ' model with the parameter $(J_1, K, \Gamma, \Gamma', J_p) = (-1.8, -7.2, 10.5, -2.5, 0.15)$ and the J_1–K–J_2–J_3 model with $(J_1, K, J_2, J_3, \Gamma', J_p) = (1.5, -8.1, 0.8, 5.8, -0.14, 0.15)$ is plotted in Fig. S8(a) and (b), respectively. In both models, the total energy is minimized at the wavevector (0, 1/2, 1) (r.l.u.) and its equivalent wavevectors. If we assume that a single-Q magnetic structure with the wavevector of $\mathbf{k} = (0, 1/2, 1)$ is realized as the ground state, the eigenvector of $H_{\mathbf{k}}$ becomes $(\mathbf{u}/\sqrt{2}, \mathbf{u}/\sqrt{2})$ ($\mathbf{u}$: unit vector). The eigenvector indicates the identical magnetic moments at the site A (2/3, 1/3, z_{Ru}) and B (1/3, 2/3, 1-z_{Ru}). The propagation vector $\mathbf{k} = (0, 1/2, 1)$ combined with the equivalent magnetic moments at the two sites supports the realization of a zigzag antiferromagnetic structure[6]. The unit vector $\mathbf{u}$ represents the direction of the magnetic moments in the antiferromagnetic order, which forms an angle of 32° and 55° from the honeycomb plane for the J_1–K–Γ–Γ' and J_1–K–J_2–J_3 models, respectively.

Excitation energy and dynamical structure factor of four magnon modes were calculated from the eigenvalues and eigenvector obtained by diagonalizing the 8×8 Bogoliubov-de Gennes Hamiltonian. The dispersion relation and dynamical structure factor of the four modes for the J_1–K–Γ–Γ' and J_1–K–J_2–J_3 models are shown in Figs. S9(a,b). The large Γ term causes largely dispersive modes with a large dynamical structure factor at (1/2, 0, 0) in the J_1–K–Γ–Γ' model, while the large J_3 term causes the similar dispersive mode at both (1/2, 0, 0) and (0, 1/2, 0) in the J_1–K–J_2–J_3 model. The origin of the dispersion would be revealed easily if inelastic neutron scattering experiments using the single crystalline samples became possible.

At last, the spectrum was averaged over the whole solid

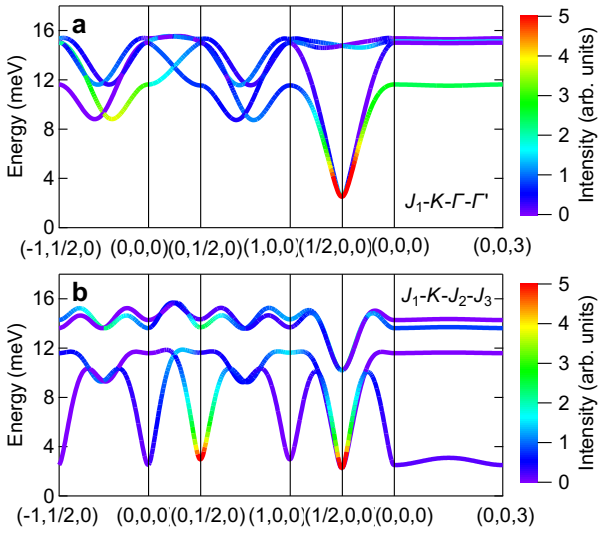

FIG. S9. Dispersion relation and dynamical structure factor expected from the linear spin wave calculations on (a) the J_1–K–Γ–Γ' and (b) J_1–K–J_2–J_3 models.

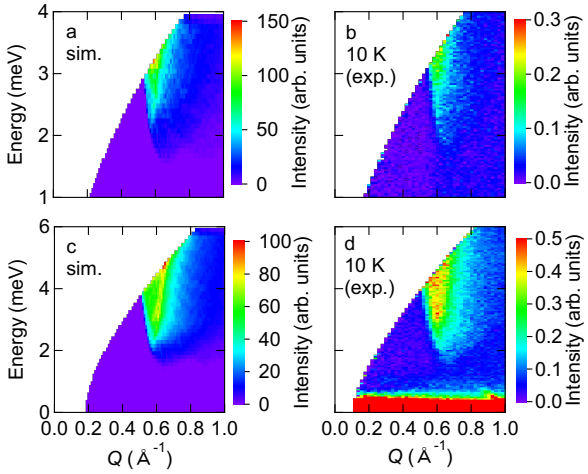

FIG. S10. Powder neutron scattering spectra calculated for the J_1–K–J_2–J_3 model compared with the experimental spectra. (a) Calculated spectra for $E_i = 5.57$ meV. (b) Experimental spectra collected for $E_i = 5.57$ meV. (c) Calculated spectra for $E_i = 9.70$ meV. (d) Experimental spectra collected for $E_i = 9.70$ meV.

angle and convoluted by the wavevector and energy resolutions estimated by the analytic method[13]. For instance, the inelastic neutron scattering spectra calculated for the J_1–K–J_2–J_3 model are shown in Fig. S10(a) and (c). These spectra were convoluted by the wavevector and energy resolutions expected for $E_i = 5.57$ and 9.70 meV, respectively. The spectra collected at 10 K (enlarged figures of Figs. S1(a) and S2(a)) are shown in Fig. S10(b) and (d) for comparison. The interplane interactions of $J_p = 0.15$ meV were determined so that the calculated spectra well reproduce the observed low-energy excitations. Figures 5(a,b) in the main text were also obtained in the same manner using $E_i = 20.95$ meV.

---

* Present address: Neutron Science and Technology Center, Comprehensive Research Organization for Science and Society (CROSS), Tokai, Ibaraki, 319-1106, Japan

† Present address: Institute of Materials Structure Science (IMSS), High Energy Accelerator Research Organization (KEK), Ibaraki, 305-0801, Japan.

[1] K. Nakajima, S. Ohira-Kawamura, T. Kikuchi, M. Nakamura, R. Kajimoto, Y. Inamura, N. Takahashi, K. Aizawa, K. Suzuya, K. Shibata, T. Nakatani, K. Soyama, R. Maruyama, H. Tanaka, W. Kambara, T. Iwahashi, Y. Itoh, T. Osakabe, S. Wakimoto, K. Kakurai, F. Maekawa, M. Harada, K. Oikawa, R. E. Lechner, F. Mezei, and M. Arai, Journal of the Physical Society of Japan **80**, SB028 (2011), https://doi.org/10.1143/JPSJS.80SB.SB028.

[2] M. Nakamura, R. Kajimoto, Y. Inamura, F. Mizuno, M. Fujita, T. Yokoo, and M. Arai, Journal of the Physical Society of Japan **78**, 093002 (2009).

[3] D. Yu, R. Mole, T. Noakes, S. Kennedy, and R. Robinson, Journal of the Physical Society of Japan **82**, SA027 (2013), https://doi.org/10.7566/JPSJS.82SA.SA027.

[4] D. Richard, M. Ferrand, and G. Kearley, Journal of Neutron Research **4**, 33 (1996), https://doi.org/10.1080/10238169608200065.

[5] K. Nawa, D. Okuyama, H.-C. Wu, R. Murasaki, S. Matsuzaka, K. Kinjo, and T. J. Sato, Journal of the Physical Society of Japan **93**, 091001 (2024), https://doi.org/10.7566/JPSJ.93.091001.

[6] Y. Imai, K. Nawa, Y. Shimizu, W. Yamada, H. Fujihara, T. Aoyama, R. Takahashi, D. Okuyama, T. Ohashi, M. Hagihala, S. Torii, D. Morikawa, M. Terauchi, T. Kawamata, M. Kato, H. Gotou, M. Itoh, T. J. Sato, and K. Ohgushi, Phys. Rev. B **105**, L041112 (2022).

[7] J. M. Luttinger and L. Tisza, Phys. Rev. **70**, 954 (1946).

[8] D. Litvin, Physica **77**, 205 (1974).

[9] J. G. Rau, E. K.-H. Lee, and H.-Y. Kee, Phys. Rev. Lett. **112**, 077204 (2014).

[10] J. c. v. Chaloupka and G. Khaliullin, Phys. Rev. B **92**, 024413 (2015).

[11] J. c. v. Chaloupka and G. Khaliullin, Phys. Rev. B **94**, 064435 (2016).

[12] R. L. Smit, S. Keupert, O. Tsyplyatyev, P. A. Maksimov, A. L. Chernyshev, and P. Kopietz, Phys. Rev. B **101**, 054424 (2020).

[13] R. Kajimoto, K. Sato, Y. Inamura, and M. Fujita, AIP Conference Proceedings **1969**, 050004 (2018), https://pubs.aip.org/aip/acp/article-pdf/doi/10.1063/1.5039301/14158864/050004_1_online.pdf.